

## Photo-triggering and secondary electron produced ionization in electric discharge ArF\* excimer lasers

Zhongmin Xiong<sup>a)</sup> and Mark J. Kushner<sup>b)</sup>

*Electrical Engineering and Computer Science Department, University of Michigan, 1301 Beal Avenue, Ann Arbor, Michigan 48109-2122, USA*

(Received 21 July 2011; accepted 18 August 2011; published online 19 October 2011)

Electric discharge excimer lasers are sustained in multi-atmosphere attaching gas mixtures that are typically preionized to enable a reproducible, uniform glow, which maximizes optical quality and gain. This preionization is often accomplished using UV light produced by a corona discharge within the plasma cavity. To quantify the relationship between corona discharge properties and those of the laser discharge, the triggering of electron avalanche by preionizing UV light in an electric discharge-pumped ArF\* excimer laser was numerically investigated using a two-dimensional model. The preionizing UV fluxes were generated by a corona-bar discharge driven by the same voltage pulse as the main discharge sustained in a multi-atmospheric Ne/Ar/Xe/F<sub>2</sub> gas mixture. The resulting peak photoelectron density in the inter-electrode spacing is around  $10^8 \text{ cm}^{-3}$ , and its distribution is biased toward the UV source. The preionization density increases with increasing dielectric constant and capacitance of the corona bar. The symmetry and uniformity of the discharge are, however, improved significantly once the main avalanche develops. In addition to bulk electron impact ionization, the ionization generated by sheath accelerated secondary electrons was found to be important in sustaining the discharge current at experimentally observed values. At peak current, the magnitude of the ionization by sheath accelerated electrons is comparable to that from bulk electron impact in the vicinity of the cathode.

© 2011 American Institute of Physics. [doi:10.1063/1.3644953]

### I. INTRODUCTION

With a short wavelength (193 nm), high repetition rate, and high power output, electric discharge-excited ArF\* excimer lasers are widely used in micro-electronics fabrication for optical lithography,<sup>1,2</sup> corneal refractive surgery,<sup>3,4</sup> pulsed laser ablation<sup>5,6</sup> and plasma-assisted ignition and combustion.<sup>7,8</sup> To efficiently pump the laser with high optical quality, the discharge should operate in a volumetrically diffuse or glow discharge mode.<sup>9</sup> This mode of operation is typically accomplished by preionizing the gas mixture using an ultraviolet (UV) or x-ray radiation source. Sufficient preionization electron density, typically  $10^8$ – $10^{10} \text{ cm}^{-3}$ , prevents the rapid formation of streamers and delays their subsequent transition to arcs.<sup>10–13</sup> The density and uniformity of the photoelectrons and timing of the preionization directly affect the laser's performance.<sup>12</sup> There are at least two preionization schemes. The first is command-charging where preionization photons are produced by a separate discharge circuit than the laser discharge, and so the timing between the production of preionization and application of avalanching voltage across the main electrodes can be independently set. The second approach is photo-triggering. In this method, voltage is already across the main discharge gap when the photoelectrons are produced. The avalanche is then triggered by the preionization. Often the electrical circuits for both the preionization and discharge pulses are driven by the same applied voltage.

While its importance to excimer lasers is well recognized, the consequences of preionization on the development of the discharge is not well quantified. It is well known that an adequate initial photo-electron density is critical to maintaining a stable and homogeneous discharge. The threshold density for preionization to provide a uniform glow discharge in attaching gases was estimated by Lavatter and Lin.<sup>11,13</sup> In their model, the minimum preionization density for a uniform glow is the value for which the lateral diffusion of avalanches seeded by individual photo-electrons enables their overlap into a uniform glow prior to crossing the discharge gap. This minimum value is of  $10^8$ – $10^9 \text{ cm}^{-3}$  for many excimer laser mixtures.

Insufficient or strongly non-uniform preionization can trigger discharge instabilities. Using the UV radiation from a KrF\* laser to preionize a XeCl\* laser, Taylor<sup>15</sup> found that discharge instabilities begin in the form of cathode spots, which then grow into filaments in response to preionization gradients. Eventually these filaments bridge the electrode gap and terminate the optical pulse earlier than the current pulse (which is now carried through many arc-like filaments). The initial development of the filaments has been identified with halogen donor depletion.<sup>16</sup> In excimer lasers using F<sub>2</sub> as the halogen donor (e.g., KrF\*, ArF\*, F<sub>2</sub>\*) Mathew *et al.*<sup>17</sup> found that the current filamentation is not associated with cathode spots but emerges from the bulk glow discharge. Above the threshold preionization density for a uniform glow, the output energy of XeCl\* excimer lasers typically increases monotonically with preionization density, until an saturation level is reached when the photoelectron density exceeds  $10^9 \text{ cm}^{-3}$ .<sup>13,14</sup>

<sup>a)</sup>Electronic mail: zxiong@umich.edu.

<sup>b)</sup>Author to whom correspondence should be addressed. Electronic mail: mjkuhs@umich.edu.

In global modeling of KrF\* and ArF\* lasers, Greene and Brau<sup>18</sup> used a preionization density of  $n_{e0} = 10^8 \text{ cm}^{-3}$  and obtained good agreement with experiments for the time evolution of the discharge voltage and current. Akashi, Sakai, and Tagashira<sup>19,20</sup> used a one-dimensional model to investigate an ArF\* laser while varying the preionization densities,  $n_{e0}$ . They found that as  $n_{e0}$  decreased, the peak values of discharge voltage and current were delayed but eventually became larger, which then leads to a higher density of ArF\*. This modeling did not consider the propensity for forming micro-arcs at low preionization density. The need for spatially uniform preionization over large volumes motivated research into using x-rays as preionization sources.<sup>21,22</sup> In such cases, a decreasing preionization density can produce a higher ArF\* density if the electrons can be supplied homogeneously in the gap. Optimizing photoionization sources can also influence the choice of the gas mixture. For example, it has been found that adding a small amount of low-ionization potential gases (such as Xe, O<sub>2</sub>) to a fluorine-based excimer laser gas mixture can substantially increase the preionization density and produce longer stable glow discharges. Adding larger amounts of Xe to the point of intercepting significant amount of discharge power decreases laser power output.<sup>23,24</sup>

In models of excimer lasers, photon produced preionization has typically been represented by a spatially uniform initial electron density at the time the voltage pulse is applied. In photo-triggering, preionization is a dynamic process that can have significant and mutual influence on the main laser discharge it triggers. For example, with many corona-bar preionization sources, UV photons are produced by a surface discharge that is driven by the same voltage pulse as the main discharge. The production of the UV light by the corona bar significantly overlaps with the discharge itself. The density and distribution of the photo-produced electrons depends critically on the timing, strength, propagation characteristics of the corona discharge across its surface. To numerically investigate these photo-triggering processes and the characteristics of the subsequent laser discharge, the corona and laser discharges driven by the same voltage pulse should be simultaneously addressed. Results from such integrated models can provide insights to improving the discharge uniformity and the performance of the laser.

In this paper, we present results from a two-dimensional numerical investigation of the photo-triggering of an electric discharge excited ArF\* excimer laser. The triggering UV photons are produced by a corona bar discharge in a multi-atmosphere Ne/Ar/F<sub>2</sub>/Xe gas mixture. First, the density and distribution of the photoelectrons produced by the UV light are presented in conjunction with the development of the corona bar discharge and the subsequent main avalanche. The densities of electrons, ions, and excited states in the discharge and their uniformity are discussed. Second, sheath accelerated secondary electrons from the cathode are found to provide significant ionization that is important to determining the total discharge current. Finally, the consequences of varying of the dielectric constant of the corona bar was investigated, and we found that higher dielectric constants produced larger fluxes of preionizing UV photons and so triggered the main discharge more rapidly. The optimum

concentration of the halogen donor F<sub>2</sub> gas was also investigated.

The governing equations and the model are briefly described in Sec. II. In Secs. III–IV, results from the simulation for dynamics of the discharge, UV light production and effects of secondary electrons are discussed. Section V contains our concluding remarks.

## II. DESCRIPTION OF THE MODEL

The modeling of the generation of preionizing UV light and the subsequent triggering of gas discharge in an ArF\* excimer laser was performed with *nonPDPSIM*, a 2-dimensional plasma hydrodynamics model with radiation photon transport. The model is the same as the one used in the study of corona bar discharges described in Ref. 25 and so will be only briefly described here.

In *nonPDPSIM*, continuity equations for charged and neutral species and Poisson's equation for electric potential are coincidentally integrated in time with the electron energy equation whose transport coefficients are obtained from stationary solutions of Boltzmann's equation. A Monte Carlo simulation is used to track sheath accelerated electrons produced by secondary processes at surfaces. The spatial discretization in *nonPDPSIM* is based on finite volume methods on an unstructured mesh and the time integration of Poisson's equation and charged particle transport is implemented with a fully implicit Newton iteration method. During the short duration of the plasma discharge, advective motion of neutral species by temperature or pressure gradients is not important. As such, after the charged species are updated, the densities of neutral species are given by their continuity equations with only diffusion for transport.

Photon transport in the plasma is accounted for using a propagator method. The photoionization source for species  $m$  at location  $\vec{r}_i$  due to the emission of photons at location  $\vec{r}_j$  by species  $k$  is

$$S_m(\vec{r}_i) = \sigma_{km}^I N_m(\vec{r}_i) A_k \int N_k(\vec{r}_j') G_k(\vec{r}_j', \vec{r}_i) d^3 \vec{r}_j', \quad (1)$$

$$G_k(\vec{r}_j, \vec{r}_i) = \frac{\exp\left(-\int_{\vec{r}_j}^{\vec{r}_i} \sum_l \sigma_{lk} N_l(\vec{r}_n') d\vec{r}_n'\right)}{4\pi |\vec{r}_i - \vec{r}_j|^2}, \quad (2)$$

where  $N_k$  is the density of the radiating species having Einstein coefficient  $A_k$ ,  $\sigma_{km}^I$  is the photoionization cross section for species  $m$  by photons emitted by species  $k$ , and  $\sigma_{lk}$  is the total absorption cross section for photon  $k$  by species  $l$ .  $G_k(\vec{r}_j, \vec{r}_i)$  is a Green's function for the survival of the photons emitted at the location  $\vec{r}_j$  to reach location  $\vec{r}_i$ , which also accounts for view angles and geometric obscuration.

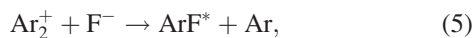
Emission of electrons from the dielectric surface results from two processes: secondary electron emission by ion bombardment and by excited states, and photoelectron emission. (The values of the electric fields are not large enough for field emission to be important.) In the present study, we focused on the secondary surface emission due to ion bombardment and the photoelectron emission was neglected. A

secondary electron emission coefficient of 0.15 was used for all ions unless otherwise noted.

In this investigation, the source of UV photons was emission by  $\text{Ne}_2^*$  with a wavelength of 85 nm (14.6 eV). The rationale for this choice is that there is moderately rapid conversion of Ne excited states to the dimer and the bound-free transition producing this radiation is not resonantly absorbed. The single photoionization process we included was for ground state xenon with cross section  $10^{-16} \text{ cm}^2$ . Although in the actual gas mixture, there are likely other photoionization processes and other sources of UV photons, we believe this choice of photon source and photoionized species represents the general scaling laws of photo-triggered discharges. Although the radiative lifetime of  $\text{Ne}_2^*$  is only 11 ns, the precursor states for forming  $\text{Ne}_2^*$  are metastable excited states (or effectively metastable due to radiation trapping) and so the source of 85 nm photons can last for times considerably longer than the  $\text{Ne}_2^*$  lifetime. The UV photon from  $\text{Ne}_2^*$  is capable of directly ionizing only Xe in the feedstock gas mixture that has an ionization potential of 12.1 eV. The radiation is essentially transparent in unexcited Ne due to the lack of resonance trapping.

The trajectories of secondary electrons emitted from surfaces are followed using an electron Monte Carlo simulation (eMCS), which is described in detail in Ref. 26. Statistics on the trajectories of the emitted electrons and electrons resulting from their ionizing collisions are collected to compute electron energy distributions (EEDs) as a function of position. These EEDs are then used to compute electron impact source functions and sources of secondary electrons. These electron impact sources are included in the continuity equations for charged and neutral species in the fluid portion of the model.

In the present study, the base case gas mixture consists of  $\text{Ne}/\text{Ar}/\text{F}_2/\text{Xe} = 96.4/3.5/0.1/0.001$  at a pressure of 3.5 atm and temperature 350 K. A reduced reaction mechanism was formulated that captures the dominant plasma processes without being too computationally burdensome and is essentially adopted from Refs. 27–29. The upper level of the laser species,  $\text{ArF}^*$ , is formed from its main precursors of  $\text{Ar}^*$ ,  $\text{Ar}^+$ , and  $\text{Ar}_2^+$ , and  $\text{F}_2$  or  $\text{F}^-$  by



where the negative ion is formed by electron dissociative attachment to  $\text{F}_2$ .

The model geometry shown in Fig. 1(a) represents a typical configuration of an  $\text{ArF}^*$  excimer laser system. It consists of a powered cathode (top) and a grounded anode (bottom), the latter being encased in a polymer insulator. Electrodes are separated by 1.2 cm on their vertical axis. The cathode is surrounded by a ceramic insulator with an adjacent preionizing corona bar. The shapes of the electrodes and insulators are nozzle-like to facilitate laminar gas flow required for high repetition rate operation, which is not addressed here. The external housing is grounded. The corona bar that produces the UV preionization photons, shown in Figs. 1(b)–1(c), is an annular

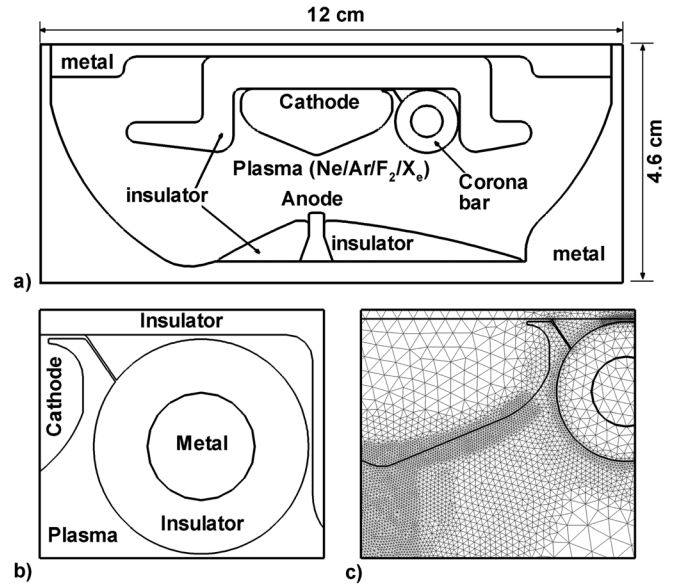


FIG. 1. Model configuration of discharge-pumped  $\text{ArF}^*$  excimer laser system. (a) Geometry, (b) corona-bar region, and (c) computational mesh near the cathode and corona bar.

dielectric tube surrounding a grounded metal rod. A metal pin connected to the powered electrode is placed on the surface of the insulator to initiate the corona discharge. There is a small clearance between the corona bar and the insulator where plasma can pass through. The inner and outer diameters of the corona bar insulator are 0.63 cm and 1.27 cm. The dielectric constant for the corona bar and electrode insulators is  $\epsilon/\epsilon_0 = 8$  unless otherwise noted. Part of the unstructured mesh used in the model is shown in Fig. 1(c). The resolution of the numerical mesh is approximately  $25 \mu\text{m}$  near the surface of the cathode and the corona dielectric. The region in which the additional ionization from the sheath accelerated secondary electrons is tracked is a rectangular area that contains the cathode's discharge facing surface and extends about 2 mm into the plasma.

The typical power supply used for excimer lasers consists of a transmission line based pulse forming network (PFN) that is connected to the cathode. The details of the driving circuit are usually complex and at the later stage of the discharge there is often ringing of the current as a result of the discharge-circuit interaction. For the present study of the photo-triggering process we chose a simplified circuit model as shown in Fig. 2(a). The values of the ballast resistor  $R_b = 0.5 \Omega$  and the head capacitance were chosen so that the cathode voltage is not significantly altered due to the circuit response to the discharge current. The applied voltage pulse is  $V(t) = V_0(1 - \cos(t/T))$ , where the pulse amplitude  $V_0 = -10 \text{ kV}$  for the base case and the pulse duration  $T = 120 \text{ ns}$ . Typical voltage and current waveforms as a function of time are shown in Fig. 2(b). The magnitude of the cathode voltage reaches its maximum at  $t = 60 \text{ ns}$  when the main discharge starts, and the discharge current reaches its peak around  $t = 90 \text{ ns}$ .

### III. CORONA-BAR DISCHARGE AND PHOTO-TRIGGERING

The photo-triggering process of the main discharge is initiated with the application of a voltage pulse simultaneously

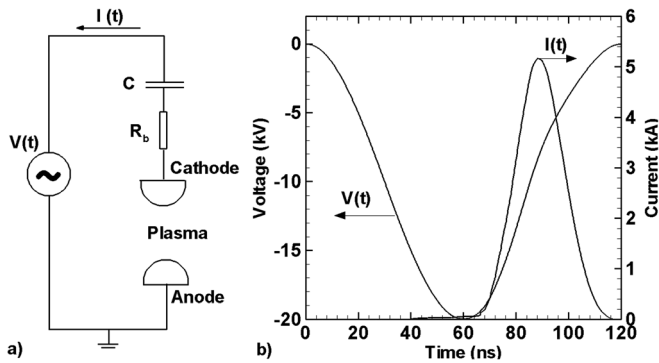


FIG. 2. Circuit parameters. (a) Simple power supply circuit model and (b) typical time history of the cathode voltage and plasma current during the photo-triggering of the ArF\* laser.

to both the cathode and the surface of the corona bar. The dynamics of isolated corona bar discharges and their UV light production are discussed in Ref. 25. In this study of a coupled corona and laser discharge, the initial electron density in the discharge chamber is zero. To initiate the corona bar discharge, a small spot of plasma is placed near the intersection of the metal pin with the corona bar. This spot of plasma is  $3 \times 10^{10} \text{ cm}^{-3}$  in density and 200 microns in diameter.

The development of the corona bar discharge is shown in Fig. 3, where the photoionization source, electron density, and the electric potential are plotted at  $t = 20, 40, 60$  and  $80$  ns. (See Fig. 2 for these timings.) The photoionization source results from the absorption by Xe atoms of 85 nm photons produced by  $\text{Ne}_2^*$ . Two separate ionization fronts are initiated on either side of the metal pin. These ionization fronts then propagate in opposite directions along the corona bar circumference. The peak electron densities inside the plasma channels behind the ionization fronts reach  $2\text{--}6 \times 10^{14} \text{ cm}^{-3}$ . The lower, counter-clockwise discharge starts earlier because it is closer to the cathode that produces a larger E/N (electric field/gas number density). This discharge reaches an average speed around the corona bar of about  $5 \times 10^7 \text{ cm s}^{-1}$ . Due to its more favorable view-angle to the main discharge gap, the preionizing UV light responsible for triggering the main discharge is produced by the lower discharge front. The upper, clockwise propagating discharge starts later due to the presence of the insulator and has a lower electron density. After passing through the narrow gap between the corona bar and insulator, the upper clockwise moving avalanche front intersects with the lower counter-clockwise propagating avalanche around  $t = 80$  ns.

During their propagation, the ionization fronts negatively charge the corona bar surface that in turn progressively charges the capacitance of the corona bar. This charging traps potential lines below the surface of the dielectric. The collision of the two fronts essentially marks the completion of the corona bar charging process. With the diminishing potential difference along the surface of the dielectric, the corona bar discharge essentially terminates at this point. The photoionization source, up to  $10^{17} \text{ cm}^{-3}\text{s}^{-1}$ , at this time is primarily from the avalanche that develops as a result of the corona bar discharge. Note that, as shown in Fig. 3, in addition to the discharge along the corona bar surface, a

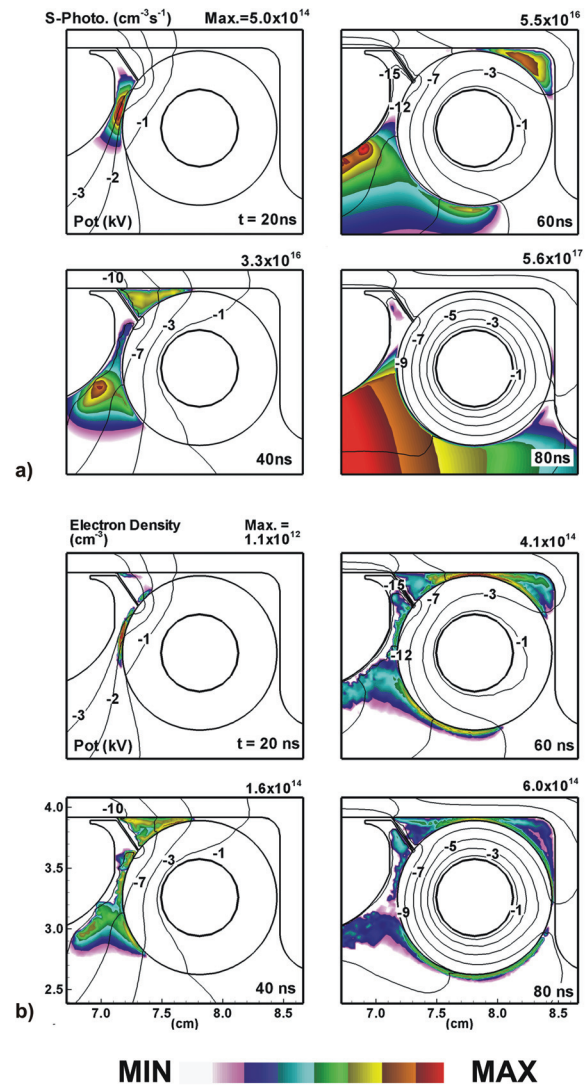


FIG. 3. (Color) Plasma properties in the vicinity of the corona bar. (a) Contours of photoionization and (b) electron density, with electric potential distribution (lines) at  $t = 20, 40, 60,$  and  $80$  ns. The discharge is first initiated in the gap between the cathode and corona bar, then propagates along the surface of the cathode and the circumference of the corona bar. The corona bar itself is progressively charged and at  $t = 80$  ns the corona bar discharge has been largely completed. The photoionization at this time comes predominantly from the main avalanche (to the left). The maximum value for each frame is noted. Flood contours are on a log scale covering 3 decades.

discharge also develops along the cathode surface that propagates toward the main discharge gap. While producing additional UV photons, this cathode-hugging discharge is heavily shadowed by the cathode itself and so the entire main discharge is not illuminated by these photons. The resulting photo-ionization contributes to the asymmetry of the main discharge as discussed below.

The photoionization source in the discharge chamber by the UV flux is shown in Fig. 4 at  $t = 45, 55, 60,$  and  $90$  ns. Since the Xe gas density is essentially uniform, the photoionization rate is directly proportional to the local UV flux. Prior to 55 ns, there is insufficient voltage across the main gap to initiate significant electron impact excitation, and so the photoionization source results from the corona bar and the cathode hugging discharge. This is during a time that the voltage is ramping up on the cathode. The spatial distribution

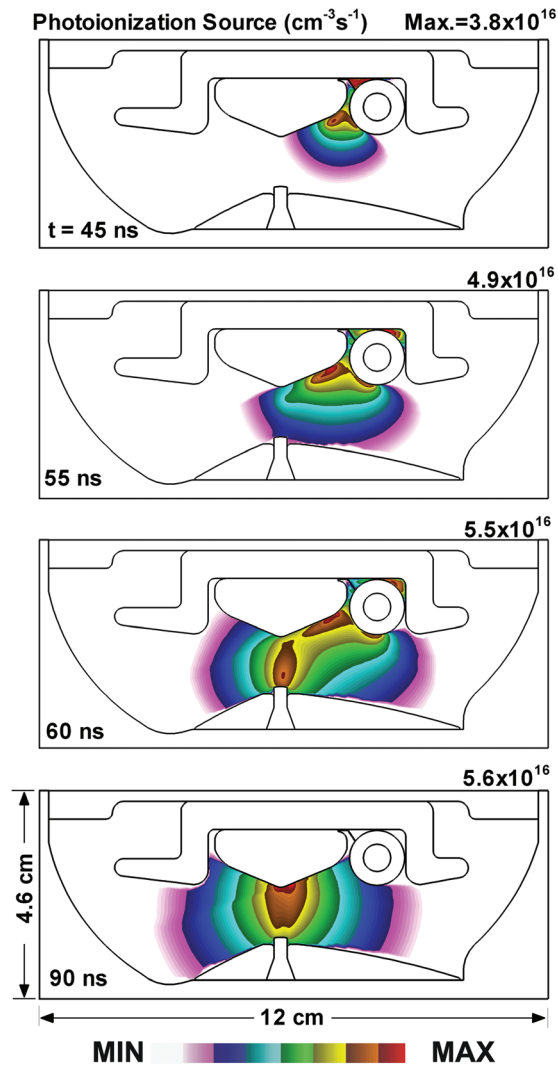


FIG. 4. (Color) Distribution of the photoionization source function at  $t = 45, 55, 60,$  and  $90$  ns. For  $t < 60$  ns, photo-electrons are generated predominantly by the UV irradiation coming from the corona bar discharge. At  $t = 90$  ns, the discharge current reaches its peak and the photoionization source is dominated by the emission generated by the main avalanche itself. The maximum value for each frame is noted. Flood contours are on a log scale covering 3 decades.

of the photoionization reflects the shadowing by the cathode. By 60 ns, avalanche has started in the main discharge gap producing comparable and larger plasma densities than in the corona discharge. Photoionization in the discharge gap is then dominated by locally produced UV photons. Once the main avalanche begins, the photoionization source becomes a superposition of contributions from the corona discharge, which gradually decays away due to the charging of the corona bar, and UV photons produced *in situ* by the avalanche itself, which grows rapidly as the avalanche proceeds.

The electron density in the entire chamber is shown in Fig. 5 at  $t = 45, 55, 60,$  and  $90$  ns. Following the photoionization sources, the regions of high electron density region start from the corona bar and spread gradually toward the main discharge gap. At  $t = 55$  ns, the time when the main avalanche begins, the electron density seeded between the main electrodes is about  $5 \times 10^{11} \text{ cm}^{-3}$ . At  $t = 60$  ns, the avalanche begins with an asymmetry in the direction of the corona bar where

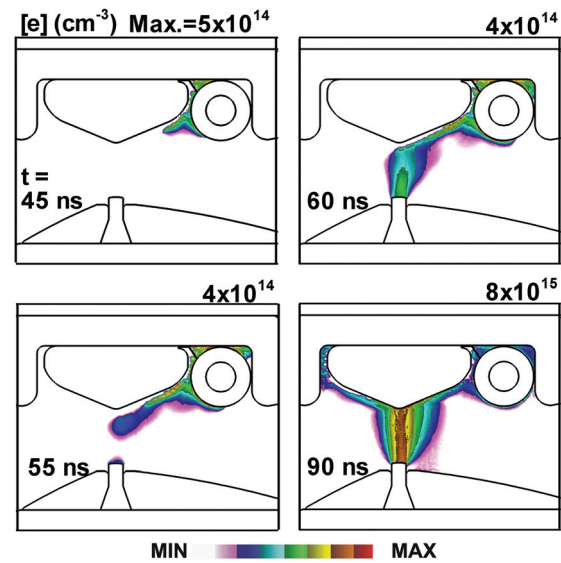


FIG. 5. (Color) Electron density during the photo-triggering process at  $t = 45, 55, 60,$  and  $90$  ns. For  $t < 60$  ns, the distribution is biased toward the corona bar and the discharge is asymmetric. At the current peak,  $t = 90$  ns, the asymmetry has been significantly reduced due to the combination of the photo-ionization generated by the main discharge itself and the sheath-accelerated secondary electrons from the cathode's plasma-facing surface. The maximum value for each frame is noted. Flood contours are on a log scale covering 4 decades.

the most intense UV flux initially comes from. The high electron density is initially concentrated close to the anode and along the face of the cathode adjacent to the corona bar as, geometrically, these locations are where the electric fields are the largest. Ionization by sheath accelerated secondary electrons resulting from ion fluxes onto the cathode contributes to the cathode hugging electron density. Geometric electric field enhancement at the narrower anode contributes to higher ionization rates there. As the avalanche develops ( $t = 90$  ns) the influence of the initial distribution of photoionization electrons diminishes and the symmetry of the electrodes begins to dominate. The discharge then becomes essentially symmetric in the region of high electron density,  $> 5 \times 10^{14} \text{ cm}^{-3}$ , where laser gain is significant.

The axial distributions of the electric field, photoionization source, electron temperature, electron density, bulk electron impact ionization source, and upper laser level  $\text{ArF}^*$  along the centerline of the main discharge at  $t = 40, 45, 50, 55,$  and  $60$  ns are shown in Figs. 6 and 7. For  $t < 50$  ns, the electric field has essentially its vacuum field configuration, uniform between the electrodes with geometric field enhancement near the electrodes. There is a negligible space charge effects on the electric potential. At  $t = 40$  ns the electron density is small ( $< 10^7 \text{ cm}^{-3}$ ) but uniform between the electrodes. The photoionization source,  $5 \times 10^{14} \text{ cm}^{-3}\text{s}^{-1}$ , is peaked toward the cathode since it is closer to the corona bar. The photoionization source is larger than the bulk electron impact ionization source. This implies that the electrons at this point are basically photoelectrons produced by the preionizing UV flux from the corona bar discharge. At  $t = 45$  ns, the bulk electron impact ionization has increased to be comparable in magnitude to that of the photoionization. The distribution of the bulk electron impact ionization source,

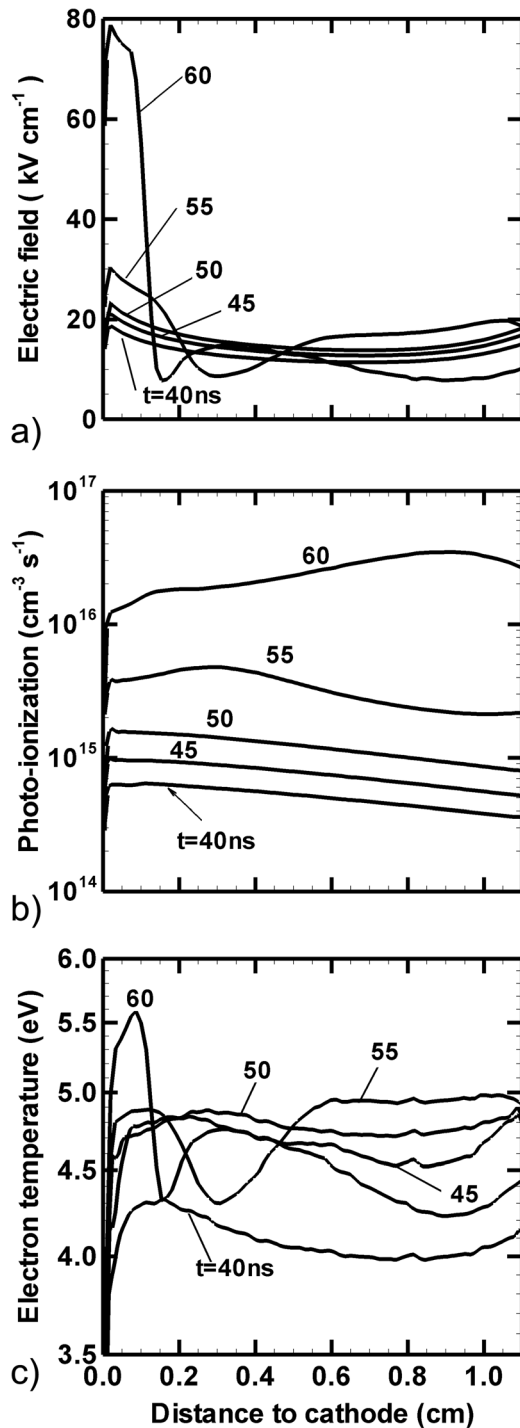


FIG. 6. Axial distribution along the centerline of the main discharge electrodes of the (a) electric field, (b) photoionization source, and (c) electron temperature at  $t = 40, 45, 50, 55,$  and  $60$  ns.

and hence the electron density, is peaked toward the cathode. The electron density at this point, is about  $10^7 \sim 10^8 \text{ cm}^{-3}$ , which would be a good approximation if one were to simply specify a preionization density. This range of values is comparable to that specified in other models.<sup>18–20</sup>

For  $t > 50$  ns, space charge begins to dominate, and the electric potential is compressed near the cathode through the formation of cathode fall. Between  $t = 50$  ns to  $60$  ns, the photo-ionization source increases by about one order of magnitude, to  $1\text{--}3 \times 10^{16} \text{ cm}^{-3}\text{s}^{-1}$  due to the local formation of

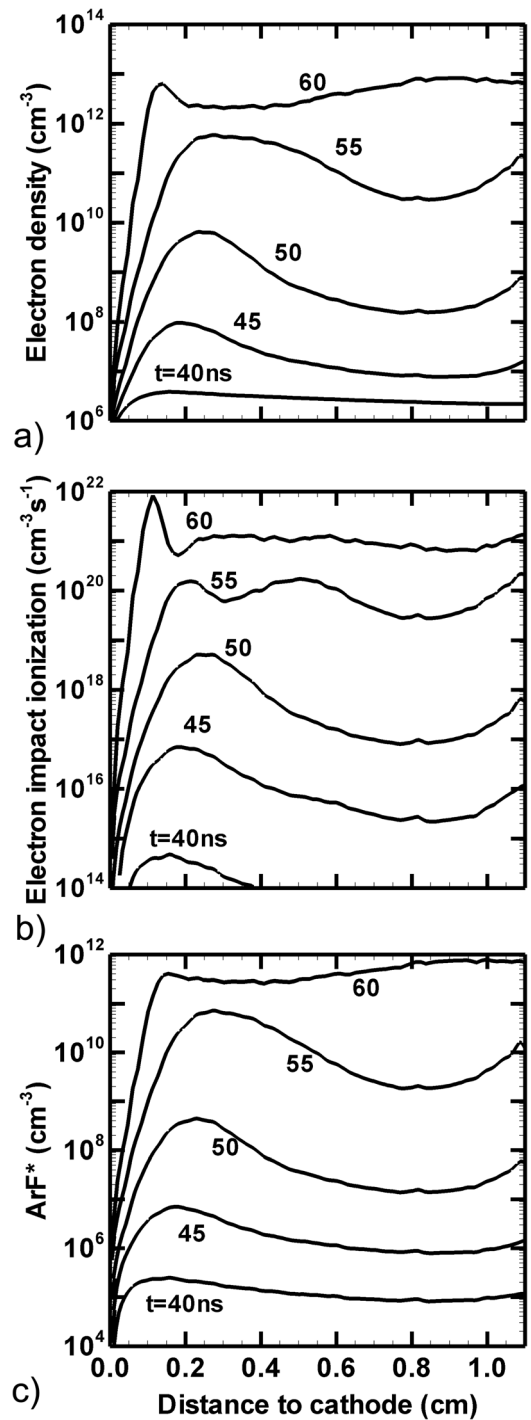


FIG. 7. Axial distribution along the centerline of the main discharge electrodes of the (a) electron density, (b) bulk electron impact ionization sources, and (c) ArF\* density at  $t = 40, 45, 50, 55,$  and  $60$  ns.

$\text{Ne}_2^*$ . However over the same time period, the bulk electron impact ionization source increases by 3–4 orders of magnitude to  $10^{21} \text{ cm}^{-3}\text{s}^{-1}$  becoming the dominant ionization source. At  $t = 55$  ns, the peak in electric field near the anode enables a rapid local increase in the electron density, which leads to a peak in excitation rates. The end result is an increase in photoionization sources.

The electron temperature  $T_e$  is between 4–6 eV and its distribution follows closely that of the electric field, reflecting the near equilibrium between  $T_e$  and the local electric

field due to the high electron collision frequency. The density of the upper laser level  $\text{ArF}^*$ , with its short 5 ns lifetime, has a spatial distribution that mirrors the production of its precursors ( $\text{Ar}^*$ ,  $\text{Ar}^+$ ), which in turn follows that of the electrons. The  $\text{ArF}^*$  lacks the near electrode maximum displayed by the electrons. This results from ionization close to the cathode having a large contribution from secondary beam electrons and being in a region of high  $T_e$ . The beam electrons preferentially produce ionization as opposed to excitation and so the neutral channel (Eq. (3)) for producing  $\text{ArF}^*$  is not emphasized. The ion-ion neutralization channel (Eq. (4)) for producing  $\text{ArF}^*$  is also not emphasized because the rate of dissociative attachment to  $\text{F}_2$  decreases with increasing  $T_e$  and is essentially zero based on the high energy secondary electrons.

At multi-atmospheric pressures, the ion and excited state densities in the discharge are dominated by the dimers. For example, the distributions of  $\text{Ne}_2^*$ ,  $\text{Ne}_2^+$ ,  $\text{Ar}_2^*$ ,  $\text{Ar}_2^+$  produced by the main avalanche at the peak current,  $t = 90$  ns, are shown in Fig. 8. While these species all follow a general spatial distribution similar to that of electrons, differences can be seen between the distributions of the ion and neutral dimers. The dimer ions border the length of the cathode while the latter do not, particularly for  $\text{Ne}_2^*$ . This implies that a large fraction of the ions are produced near the cathode by the sheath accelerated secondary electrons resulting from ion bombardment. These trends also emphasize that even in multi-atmospheric pressure discharges, sheath accelerated secondary electrons can be important to the ionization balance. This is particularly true in highly attaching gas mixtures where the lifetime of bulk electrons against attachment is short.

#### IV. SHEATH ACCELERATED SECONDARY ELECTRONS

To better quantify the additional ionization resulting from the sheath-accelerated secondary electrons, we conducted otherwise identical simulations but without the eMCS. Without the beam like electrons from the cathode, the avalanche and discharge are significantly weaker. For example, the densities of electrons and  $\text{Ar}_2^*$  at  $t = 90$  ns with and without the eMCS are compared in Fig. 9. The peak electron density is more than one order of magnitude less without the eMCS. On the other hand, the change of the densities of the dimers, such as  $\text{Ar}_2^*$  is less dramatic, a decrease of about 30% less than that with eMCS. This observation is consistent with the results shown in Fig. 8, where dimer densities are largest in the gap and so less affected by cathode processes. In the absence of ionization by secondary electrons, the discharge has additional asymmetries, which are rooted in the asymmetric illumination of the discharge gap by the corona bar. The distributions of electron and excited state densities shown in Fig. 9 without the eMCS are more biased toward the corona bar as compared to including the eMCS. The ionization by secondary electrons appears to have the added benefit of making the discharge more symmetric.

With plasma densities being sensitive to the rate of secondary electron emission the current-voltage characteristics will also be sensitive, as shown in Fig. 10(a). For  $t < 60$  ns,

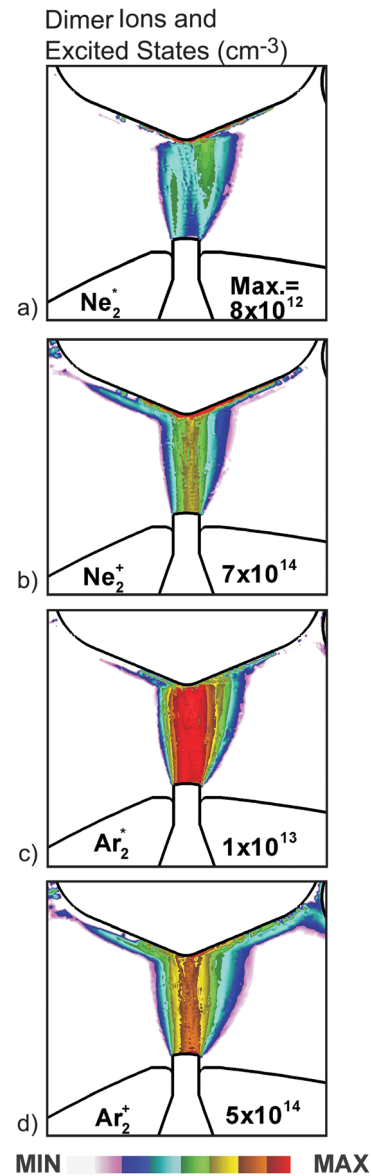


FIG. 8. (Color online) Distributions of excited state and ion dimers of Ne and Ar at the peak of the current. (a)  $\text{Ne}_2^*$ , (b)  $\text{Ne}_2^+$ , (c)  $\text{Ar}_2^*$ , (d)  $\text{Ar}_2^+$ . The ion dimers have a higher concentration than the excited species, particularly close to the cathode surface where the sheath accelerated secondary electrons provide significant additional ionization. The maximum value for each frame is noted. Flood contours are on a log scale covering 3 decades.

the current-voltage characteristics are essentially the same with and without the eMCS as significant amounts of secondary electrons have not been produced at this point. However at the peak of the avalanche,  $t = 90$  ns, the discharge current is about 5 kA with the eMCS and only around 150 A without. The larger current is consistent with experimental measurements made in similar excimer laser devices.

The secondary emission coefficient from ion bombardment used so far is  $\gamma = 0.15$ . To assess the sensitivity of the discharge performance to this choice, the secondary emission coefficient was varied from  $\gamma = 0.01 \sim 0.25$  and the resulting plasma currents are plotted in Fig. 10(b). The peak discharge current increases with increasing  $\gamma$  as the impedance of the discharge decreases. The peak current shifts to later times at low  $\gamma$  ( $< 0.1$ ) and to slightly earlier times at high values

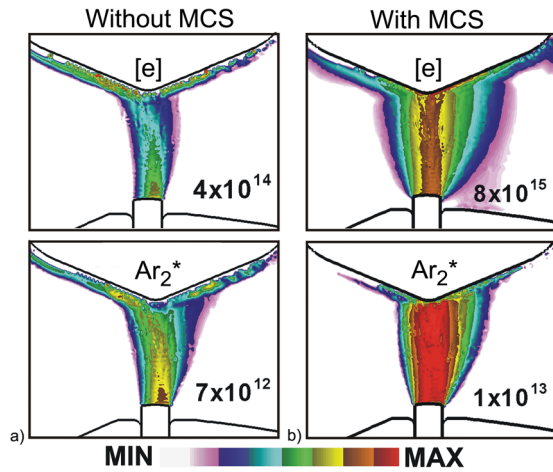


FIG. 9. (Color online) Comparisons of electron and Ar<sub>2</sub><sup>\*</sup> distributions (a) without and (b) with the additional ionization produced by sheath accelerated secondary electrons. In the latter case, the densities are significantly lower and distributions more asymmetric. The maximum value for each frame is noted. Flood contours are on a log scale covering 3 decades.

(>0.1). At low  $\gamma$  ( $< 0.1$ ), the plasma current is initially determined by bulk electron impact ionization. When this current reaches its peak, the secondary electron emission starts to become important and the combined current resulting from this additional ionization source continues to rise. On the other hand, when the  $\gamma$  is sufficiently high, the ionization providing the peak current is dominated by the secondary electron emission (see discussion below). However, with the larger plasma current, the cathode voltage collapses more rapidly (as shown in Fig. 10(a)) shifting the current peak to earlier times.

The relative contributions to ionization from the bulk and sheath accelerated secondary electrons are shown in Fig. 11 for  $\gamma = 0.05$  and 0.15. For  $\gamma = 0.05$  at  $t = 70$  ns, the initial stage of the main avalanche, the contribution from the bulk electrons is within a factor of two from that of secondary electrons on a peak basis. This is primarily due to the relatively small ion current at this stage. At the peak current,  $t = 90$  ns, the contributions from secondary electrons are comparable to that from the bulk electrons. For  $\gamma = 0.15$ , the contribution to ionization from the secondary electrons is about the same as at  $t = 70$  ns and exceeds that from the bulk electrons at  $t = 90$  ns. This increasing contribution from secondary electrons is due in large part to the cumulative increase in the ion current to the surface, which, with a large cathode sheath voltage drop ( $\sim 10$  kV at  $t = 70$  ns), produces more high energy secondary electrons with a longer range into the gas. In any case, the ionization source from the secondary electrons is concentrated near the cathode surface, reflecting the short mean free path of the energetic secondary electrons, on the order of 1 mm.

One of the important design parameters of the preionizer is the dielectric constant  $\epsilon/\epsilon_0$  of the corona bar. The increase in  $\epsilon/\epsilon_0$  and corresponding increase in capacitance of the corona bar enables a longer, more intense source of UV photons.<sup>25</sup> With the longer charging time with increasing  $\epsilon/\epsilon_0$ , the voltage applied to the corona bar is larger prior to the bar being fully charged. This produces more rapid photoionization earlier in the voltage pulse, lowering the impedance of

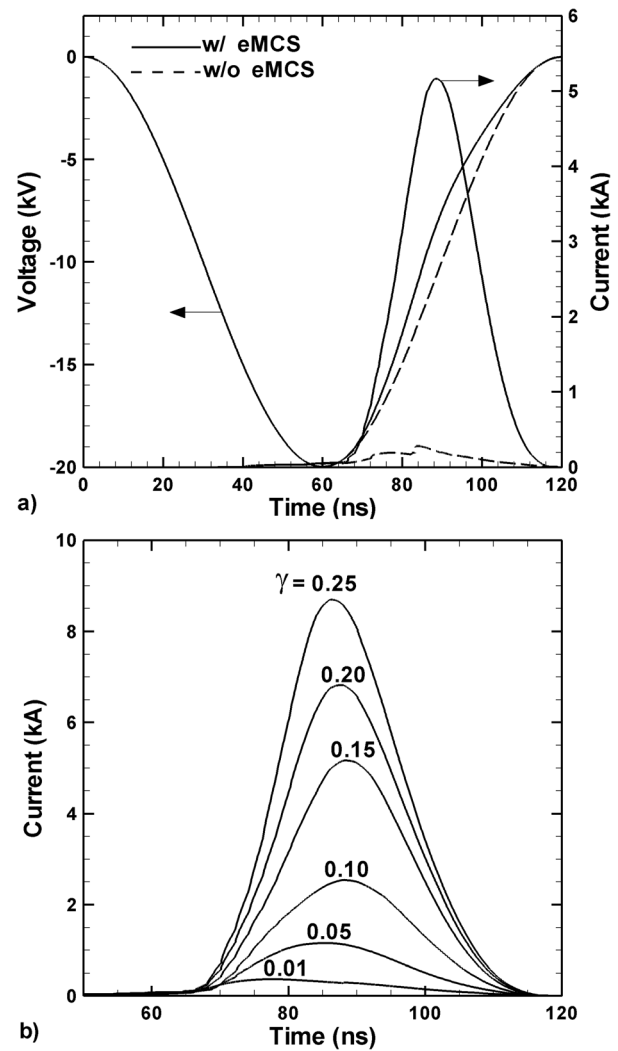


FIG. 10. Comparisons of the discharge V-I characteristics (a) with and without sheath accelerated secondary electrons and (b) discharge currents with different secondary emission coefficients  $\gamma = 0.01$ –0.25.

the discharge and increasing the discharge current. This trend is shown in Fig. 12 for  $\epsilon/\epsilon_0 = 1$ –16. With an increasing  $\epsilon/\epsilon_0$ , not only does the discharge current significantly increase, the peak current also shifts to earlier times, similar to the increasing contribution to ionization by secondary electrons with increasing  $\gamma$ . These effects are not independent since larger preionizing UV fluxes translate into larger cumulative ion current and thus more secondary electron emission from the cathode.

Another important factor determining the pumping efficiency of the ArF<sup>\*</sup> excimer laser is the concentration of the attaching gas F<sub>2</sub>. The peak discharge current and the maximum small signal gain for different F<sub>2</sub> mole fractions (0.01 – 0.20%) are shown in Fig. 13. The ArF<sup>\*</sup> density at peak current varies between  $5 \times 10^{12}$  to  $1.2 \times 10^{14}$  cm<sup>-3</sup> for different F<sub>2</sub> fractions but the inter-electrode distribution remains largely uniform. The small signal gain (ignoring absorption) was computed at the middle of the gap using a stimulated emission cross section of  $4 \times 10^{-16}$  cm<sup>2</sup>.<sup>20</sup> Increasing concentrations of F<sub>2</sub> produce a monotonic decrease of the discharge current, a consequence of the increasing rate of attachment and increasing impedance of

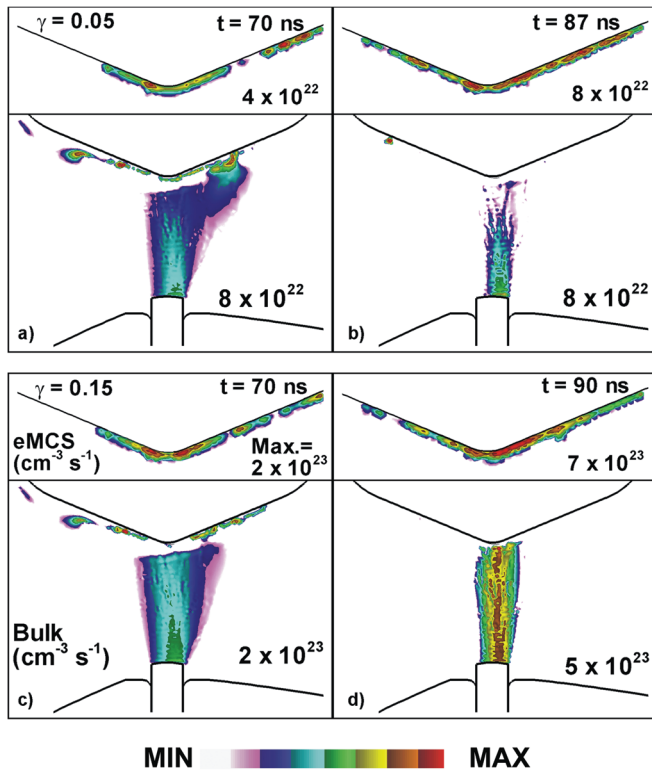


FIG. 11. (Color) The relative contributions from bulk electron impact and secondary electrons during the discharge at  $t = 70$  and  $90$  ns for secondary emission coefficients of  $\gamma = 0.05$  and  $0.15$ . For  $\gamma = 0.05$  at  $t = 70$  ns the secondary electron contribution is less than that from bulk electrons, but becomes comparable at  $t = 90$  ns. For  $\gamma = 0.15$ , the contribution from secondary electrons is comparable to bulk ionization to  $t = 70$  ns and exceeds that from bulk electron at  $t = 90$  ns. The maximum value for each frame is noted. Flood contours are on a log scale covering 3 decades.

the discharge. On the other hand, there is an optimum  $F_2$  concentration around  $0.08\%$  where the small signal gain is maximum at  $0.048 \text{ cm}^{-1}$ . This results from a trade-off between increasing rates of production of  $F^-$  and availability of  $F_2$  for the ion and neutral channels for formation of  $ArF^*$ , and increased quenching of  $ArF^*$  and reduced electron density.

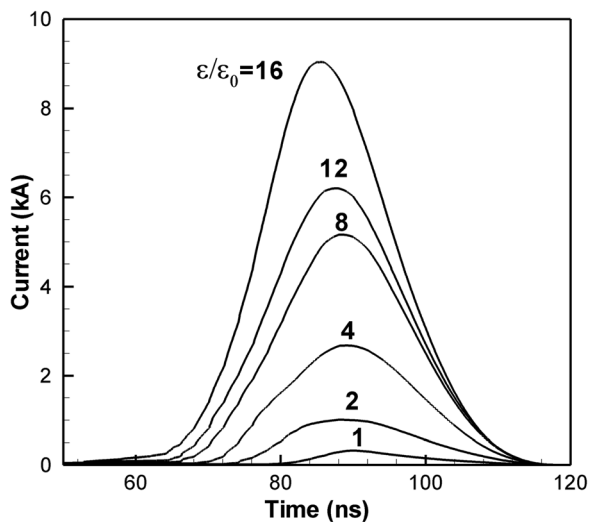


FIG. 12. Discharge currents for different dielectric constants of the corona bar,  $\epsilon/\epsilon_0 = 1-16$ .

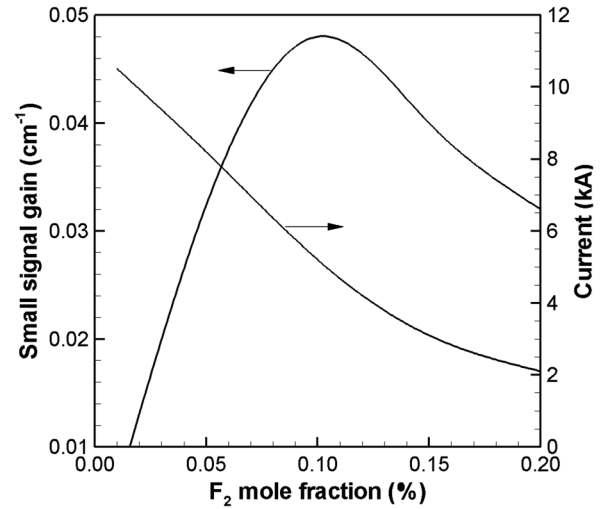


FIG. 13. The discharge current and laser small signal gain at different  $F_2$  mole fractions,  $0.01-0.20\%$ .

## V. CONCLUDING REMARKS

A numerical investigation of an excimer laser discharge triggered by photo-ionization from a corona bar in a multi-atmospheric pressure Ne/Ar/Xe/ $F_2$  gas mixture has been discussed. The corona bar discharge, driven by the same voltage pulse as for the main discharge, produces UV fluxes that photoionize Xe in the inter-electrode spacing. The pre-avalanche photo-generated electron density is about  $10^8 \text{ cm}^{-3}$ . The initial avalanche is biased toward the direction of the incoming UV flux, but as the main avalanche develops, the symmetry improves. The additional ionization produced by the sheath-accelerated secondary electrons is critical to determining the discharge current. At the peak current, the contributions from the secondary electrons to ionization in the presheath are comparable to that from the bulk electrons. The secondary electrons also help to reduce the discharge asymmetry due to the directional preionization UV fluxes. Increasing dielectric constant of the corona bar increases the total photoionization and the peak current of the main avalanche. The optimum concentration of attaching gas  $F_2$  in terms of laser pumping efficiency is around  $0.08\%$ , a consequence of a trade-off between decreasing discharge current with increasing  $F_2$  fraction and increasing utilization of the precursor to the upper laser level,  $Ar^*$ ,  $Ar^+$ , and  $Ar_2^+$ , in reacting with  $F_2$  and  $F^-$ .

## ACKNOWLEDGMENTS

This work was supported by Cymer, Inc. and the Department of Energy Office of Fusion Energy Sciences. The authors thank Dr. Thomas Duffey for his insights and his advice.

<sup>1</sup>R. Rubingh, M. Moers, M. Suddendorf, P. Vanoppen, A. Kisteman, M. Thier, V. Blahnik, E. Piper, *Proc SPIE* **5754**, 681 (2005).

<sup>2</sup>N. Irie, M. Hamatani, and M. Nei, *Proc. SPIE* **5754**, 725 (2005).

<sup>3</sup>C. N. J. McGhee, H. R. Taylor, D. S. Gartr, and S. L. Trokel, *Excimer Lasers in Ophthalmology: Principles and Practice* (Martin Duntz, London, 1997).

<sup>4</sup>E. E. Manche, J. D. Carr, W. W. Haw, and P. S. Hersh, *West. J. Med.* **169**, 30 (1998).

- <sup>5</sup>S. Amoruso, R. Bruzzese, N. Spinelli, and R. Velotta, *J. Phys. B: At. Mol. Opt. Phys.* **32**, R131 (1999).
- <sup>6</sup>*Pulsed Laser Deposition of Thin Films* (Wiley, New York, 1994).
- <sup>7</sup>M. Lavid, Y. Nachshon, S. K. Gulati, and J. G. Stevens, *Combust. Sci. Technol.* **96**, 231 (1994).
- <sup>8</sup>J. X. Ma, D. R. Alexander, and D. E. Poulain, *Combust. Flame* **112**, 492 (1998).
- <sup>9</sup>H. S. W. Massey, W. McDaniel, and B. Bederson, *Applied Atomic Collision Physics*, Vol. 3: Gas Lasers (Academic, New York, 1982).
- <sup>10</sup>R. C. Sze and T. R. Loree, *IEEE J. Quant. Electron.* **QE-14**, 944 (1978).
- <sup>11</sup>J. I. Levatter and S. C. Lin, *J. Appl. Phys.* **51**, 210 (1980).
- <sup>12</sup>L. Feenstra, O. B. Hoekstra, P. J. M. Peters, and W. J. Witteman, *Appl. Phys. B* **70**, 231 (2000).
- <sup>13</sup>S. C. Lin and J. I. Levatter, *Appl. Phys. Lett.* **34**, 505 (1979).
- <sup>14</sup>B. Lacour and C. Vannier, *J. Appl. Phys.* **62**, 754 (1987).
- <sup>15</sup>R. S. Taylor, *Appl. Phys. B* **41**, 1 (1986).
- <sup>16</sup>J. Coutts and C. E. Webb, *J. Appl. Phys.* **59**, 704 (1986).
- <sup>17</sup>D. Mathew, H. M. J. Bastiaens, K.-J. Boller, and P. J. M. Peters, *J. Appl. Phys.* **102**, 033305 (2007).
- <sup>18</sup>A. E. Greene and C. A. Brau, *IEEE J. Quant. Electron.* **QE-14**, 951 (1978).
- <sup>19</sup>H. Akashi, Y. Sakai, and H. Tagashira, *J. Phys. D: Appl. Phys.* **27**, 1097 (1994).
- <sup>20</sup>H. Akashi, Y. Sakai, and H. Tagashira, *J. Phys. D: Appl. Phys.* **28**, 445 (1995).
- <sup>21</sup>J.-M. Hueber, B. L. Fontaine, P. C. Delaporte, B. M. Forestier, and M. L. Senties, *Optics Commun.* **85**, 237 (1991).
- <sup>22</sup>C. H. Fisher, M. J. Kushner, T. E. Dehart, J. P. McDaniel, R. A. Petr, and J. J. Ewing, *Appl. Phys. Lett.* **48**, 1574 (1986).
- <sup>23</sup>N. Kataoka, M. Itagaki, K. Uchino, K. Muraoka, A. Takahashi, T. Okada, M. Maeda, T. Ori, K. Terashima, A. Sumitani, T. Enami, and H. Mizoguchi, *Jpn. J. Appl. Phys.* **38**, 6735 (1999).
- <sup>24</sup>D. Mathem, P. J. M. Perters, H. M. J. Bastiaens, and K.-J. Boller, *Appl. Phys. B: Laser Opt.*, **95**, 155 (2009).
- <sup>25</sup>Z. Xiong and M. J. Kushner, *J. Phys. D: Appl. Phys.* **43**, 505204 (2010).
- <sup>26</sup>M. J. Kushner, *J. Appl. Phys.* **95**, 846 (2004).
- <sup>27</sup>S. Rauf and M. J. Kushner, *J. Appl. Phys.* **85**, 3460 (1999).
- <sup>28</sup>F. Kannari, M. Obara, and T. Fujioka, *J. Appl. Phys.* **57**, 4309 (1985).
- <sup>29</sup>M. Ohwa and M. Obara, *J. Appl. Phys.* **59**, 32 (1986).